Observation of Non-Abelian Charged Nodes Linking Nonadjacent Gaps

Dongyang Wang[1], Biao Yang[1,2] Mudi Wang[1], Ruo-Yang Zhang[1], Xiao Li[1], Z. Q. Zhang[1],
Shuang Zhang[3,4,*] and C. T. Chan[1,†]

[1]*Department of Physics and Center for Metamaterials Research, Hong Kong University of Science and Technology,
Hong Kong, China*
[2]*College of Advanced Interdisciplinary Studies, National University of Defense Technology,
Changsha 410073, China*
[3]*Department of Physics, The University of Hong Kong, Hong Kong, China*
[4]*Department of Electrical and Electronic Engineering, The University of Hong Kong, Hong Kong, China*

Nodal links are special configurations of band degeneracies in the momentum space, where nodal line branches encircle each other. In PT symmetric systems, nodal lines can be topologically characterized using the eigenvector frame rotations along an encircling loop and the linking structure can be described with non-Abelian frame charges involving adjacent bands. While the commutation rules between the frame charges are well established, the underlying relationship between distant band gap closing nodes remains to be explored. In this Letter, we present a photonic multiple nodal links system, where the nodal lines of nonadjacent bands are investigated with symmetry constraints on frame charges. Through an orthogonal nodal chain, the nodal line from the lower two bands predicts the existence of nodal lines formed between the higher bands. We designed and fabricated a metamaterial, with which the multiple nodal links and the topological connection between nonadjacent nodal lines are experimentally demonstrated.

Introduction.—Topological photonics has emerged as a rapidly growing field [1–3]. Band touching or crossings in gapless topological materials can appear in momentum space as diverse forms, such as the Weyl points carrying nonzero chiral charges [4–9], and the line nodes accompanied with quantized Berry phase [10,11]. The nodal lines in momentum space are typically protected by the mirror or PT symmetries [10–12], and can appear as straight lines, rings, chains, and links [13–27]. While topological characters are usually considered within one band at a time resulting in integer topological invariants, there are recent efforts that consider simultaneously the properties of a group of adjacent bands (multiband approach) resulting in topological invariants that are elements of non-Abelian groups [28,29]. Different from conventional topological band theory that uses the geometrical phase evolution of the eigenfunctions in a single band to define bulk topological invariants (e.g., Chern number), the multiband approach considers the frame rotation of a set of orthogonal eigenvectors (three or more) in Hermitian PT-symmetric systems. Since frame rotations are described by matrixlike entities, the multiband topological invariants are not integers, but are generalized quaternions, and their multiplications are generally noncommutative making the fundamental group

non-Abelian. Such a non-Abelian approach actually predates modern topological band theory and can be traced to earlier work in classifying line defects in biaxial nematic liquid crystals [30–33]. The multiband frame rotation charges have been utilized to characterize the nodal line semimetals in the presence of PT (or C_2T) symmetry [26–29,34–49], which provide new insight into the global structure of nodal lines in the momentum space.

In a PT symmetric system, the non-Abelian frame charges characterize the Hamiltonian by examining the real eigenvectors evolution along a closed homotopy (π_1) loop in the momentum space. These discrete rotations that bring a Hamiltonian back to itself form a non-Abelian generalized quaternion group (or Salingaros group) [28,29,34,36]. For example, the π_1 loop enclosed frame charge of $q = \pm g_i$ can be understood as the $\pm\pi$ rotations of a co-plane spanned by a pair of the eigenvectors [ith and $(i + 1)$th], which corresponds to a degeneracy node or line [between the ith and $(i + 1)$th bands] encircled by the π_1 loop in the momentum space. More interestingly, 0 and 2π rotations become distinct and define the trivial and nontrivial charges that are noted as "+1" and "−1," respectively (Supplemental Material 1 [50]). The nontrivial charge of "−1" imposes extra constraints to the global nodal structure beyond the single band Berry phase description.

These non-Abelian frame charges can interact among adjacent bands through a common eigenvector and they commute with each other if the nodes are formed between distant bands [28,29]. However, the underlying topological connection between nonadjacent band nodal lines is not obvious. Here, by designing a photonic metamaterial that can be made and measured, we present a multiband system with multiple nodal links in momentum space. The Hermitian system possesses PT symmetry, and the nodal lines can be characterized using non-Abelian frame charges. By incorporating additional symmetry constraints, the topological connection between nonadjacent nodal lines is revealed. It is discovered that the configuration of nodal line formed between two lower bands explains the existence of additional nodal lines in the higher two bands via the interaction with nodal structure from intermediate bands, which established the underlying connection between nonadjacent nodal lines. To illustrate our ideas, the photonic metamaterial is fabricated, and experimentally characterized at microwave frequencies, where the predicted nodal lines have been experimentally observed.

Multiple nodal links in the momentum space.—To exhibit multiple nodal links using metamaterials, more band degrees of freedom are needed beyond the fundamental propagating modes. This can be achieved using the split ring resonators (SRRs) as shown in Fig. 1(a). As commonly used in metamaterials, the SRRs possess both electric and magnetic resonances which provide longitudinal modes that can "cross" traverse modes to form nodal rings. The SRRs in Fig. 1(a) support an electric resonance driven by E_y and a magnetic resonance driven by H_z. Here, the E_x response can be neglected since the resonance frequency is much higher than the frequency regime of interest. The orientation of such two SRRs ensures the cancelation of bi-anisotropic couplings, i.e., M_1 and M_2 in Fig. 1(a) cancel out, which keeps the PT symmetry intact.

An effective medium description of the proposed SRR array results in the following constitutional parameters in the long wavelength limit as $\varepsilon = [1, \varepsilon_{yy}, 1]$ and $\mu = [1, 1, \mu_{zz}]$, with $\varepsilon_{yy} = 1 + \{[2l^2]/[L(\omega_0^2 - \omega^2)]\}$ and $\mu_{zz} = 1 + (1/\omega_0^2 - \omega^2)(2\omega^2 A^2/L)$ (Supplemental Material 2 [50]), where we have set the nonresonant components to be unity for simplicity. Based on these effective parameters, we calculated the band dispersion as shown in Fig. 1(b). The resonances of ε_{yy} and μ_{zz} introduce two longitudinal modes at the frequencies of ω_1 and ω_2 marked as stars. The longitudinal modes appear as flat bands along the k_y and k_z directions in Fig. 1(b), which intersect the transverse mode, forming into degeneracies marked with colored dots. The two frequencies of ω_1 and ω_2 correspond to the positions where the effective

Bands: ▬ 1st / 2nd ▬ 2nd / 3rd ▬ 3rd / 4th ▪▪▪ π_1 loops   Polarization band: ▬ 1st ▬ 2nd
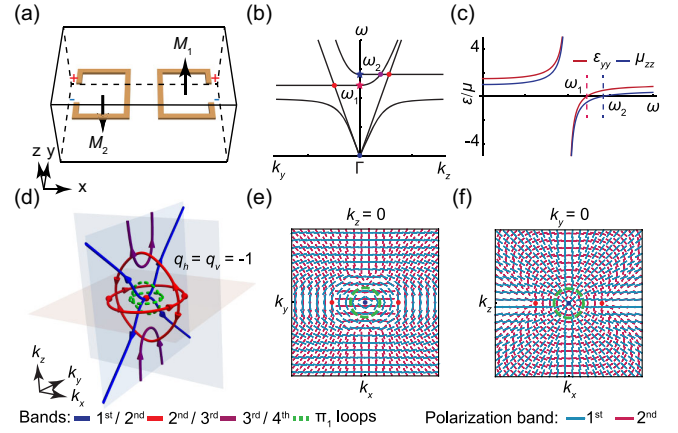
FIG. 1. Multiple nodal links in the momentum space. (a) Resonators for building multiple nodal links. The bianisotropic couplings in two rings cancel out. (b) Band dispersions along the k_y and k_z directions. Degeneracy points are colored consistent with nodal lines. The adopted parameters are $l = 1$, $A = 0.5$, $\omega_0 = 2$, $\omega_{px,y,z} = 0$. (c) Dispersions of ε_{yy} and u_{zz}, the frequencies at the zero values correspond to the flat bands in (b). (d) Nodal structure in momentum space, and multiple nodal links are formed. The two π_1 loops define the "double -1" charge at the Γ point. (e)–(f) 2π eigenpolarization state rotations for the 1st and 2nd bands on the $k_z = 0$ and $k_y = 0$ planes, verifying the "double -1" charge.

parameters ε_{yy} and μ_{zz} go to zero and the effective medium becomes near-zero material [51], as confirmed by the dispersions of the constitutional parameters in Fig. 1(c).

We then retrieve the band degeneracy positions and show the results in the momentum space as Fig. 1(d), where multiple nodal links are found. In 3D momentum space, the intersections between the flat bands and the transverse mode form into two red nodal rings (formed between the 2nd and 3rd bands) in the perpendicular planes of $k_y = 0$ and $k_z = 0$, respectively. The two nodal rings touch at the k_x axis and form as an orthogonal nodal chain in Fig. 1(d), where the intersecting modes coalesce along the k_x direction as $\omega_a = \sqrt{k_x^2}$ and $\omega_b = \sqrt{k_x^2}/\sqrt{\varepsilon_{yy}}\sqrt{\mu_{zz}}$ (Supplemental Material 3 [50]). As can be noticed from Fig. 1(d), the blue nodal line (formed between the 1st and 2nd bands) threads through the orthogonal nodal chain in the momentum space. In addition, another pair of purple nodal lines (formed between the 3rd and 4th bands) also links with the orthogonal nodal chain in red. These nodal lines together form into the multiple nodal links in momentum space.

Non-Abelian frame charges.—The multiple nodal links in the metamaterial can be characterized by non-Abelian frame charges. The Maxwell equations describing the metamaterial at low frequency can be encoded into an effective Hamiltonian as (Supplemental Material 4 [50]),

$$H = \begin{bmatrix} \frac{k_y^2}{1-2A^2} + k_z^2 + \omega_{px}^2 & \frac{k_x k_y}{-1+2A^2} & -k_x k_z & 0 & \frac{\sqrt{2}A\omega_0 k_y}{-1+2A^2} \\ \frac{k_x k_y}{-1+2A^2} & \frac{k_x^2}{1-2A^2} + k_z^2 + 2l^2 + \omega_{py}^2 & -k_y k_z & -\sqrt{2}\omega_0 & \frac{\sqrt{2}A\omega_0 k_x}{1-2A^2} \\ -k_x k_z & -k_y k_z & k_x^2 + k_y^2 + \omega_{pz}^2 & 0 & 0 \\ 0 & -\sqrt{2}\omega_0 & 0 & \omega_0^2 & 0 \\ \frac{\sqrt{2}A\omega_0 k_y}{-1+2A^2} & \frac{\sqrt{2}A\omega_0 k_x}{1-2A^2} & 0 & 0 & \frac{\omega_0^2}{1-2A^2} \end{bmatrix},$$

where the parameters ω_{px}, ω_{py}, and ω_{pz} are introduced as perturbations.

Using the eigenvectors of the effective Hamiltonian, non-Abelian frame charges are calculated (Supplemental Material 5 [50]) and presented as colored arrows in Fig. 1(d), where the color and the direction of arrow each represents the index "i" and "$\pm$" sign of the frame charge $q = \pm g_i$. We consider two π_1 loops indicated by green dotted lines in Fig. 1(d), with one in the horizontal and the other in the vertical plane, that are both encircling the Γ point. Computation results show that the frame charges for the horizontal (q_h) and vertical loop (q_v) are both "-1." As $q_h = q_v = -1$ simultaneously, we label the frame charge at Γ as a "double -1" charge. The "double -1" charge is due to the braiding induced by electrostatic mode at photonic Γ point, as has recently been proposed for biaxial media [40], only the material isotropy here is broken by resonance terms of ε_{yy} and μ_{zz}. These frame charges are essentially non-Abelian Berry phase and can be manifested as the rotation of eigenvectors or polarizations of photonic bands. We show the polarization rotations for the 1st and 2nd bands in Figs. 1(e) and 1(f) on the two mirror planes, where the 2π rotations around the Γ point exhibit the "-1" element of the generalized quaternion (or Salingaros) group. This "double -1" charge imposes constraints on the multiple nodal links when the system is perturbed (Supplemental Material 6 [50]).

Nonadjacent nodal lines and nodal links.—One consequence of non-Abelian band topology is that the braiding of nodal lines, i.e., putting one nodal line in front of another, among adjacent bands leads to a sign change to the non-Abelian frame charge $q = \pm g_i$ in generalized quaternion (or Salingaros) group (indicated by flipping of arrow direction in the figures). Although the frame charges from distant bands are known to commute and can be characterized by generalized quaternion (or Salingaros) group [28,29,34,36], or partial frame charges [42], little effort has been devoted to reveal the connection between nonadjacent nodal lines. We now proceed to reveal such connection embedded in the multiple nodal links by taking symmetry constraints into account.

From the nodal line configuration shown in Fig. 1(d), we first isolate and show the intermediate red orthogonal nodal chain in Fig. 2(a), where an arrow configuration is assigned

representing the non-Abelian frame charges $q = \pm g_2$ (characterizing the degeneracy between the 2nd and 3rd bands). The blue (1st and 2nd band degeneracy) and purple (3rd and 4th band degeneracy) nodal lines in Fig. 1(d) all link with the orthogonal chain, resulting in the braiding of nodal lines in the momentum space. We now take into consideration the blue nodal line as in Fig. 2(b), and we present the new arrow configuration after taking account only of the braiding with the blue nodal line. We notice that the blue nodal line threads through the vertical nodal ring, and the braiding changes the direction of the arrows on the vertical nodal ring that are flowing to the left chain point, where the viewpoint (or base point for homotopy loops) can be selected as the "eye-symbol" indicated. It can then be found from Fig. 2(b) that the left and right chain points have different arrow configurations after the braiding. The difference in arrow configurations between the two chain points are, however, incompatible with the time-reversal symmetry (TRS), where topologically distinct frame charges ("$+1$" and "-1") are found for the two TRS-related π_1 loops shown in Fig. 2(b) as dashed circles. Note that the π_1 loop encircling the left chain point exhibits a charge of "-1," while the π_1 loop encircling the right chain point forms a charge of "$+1$." As "-1" and "$+1$" belong to different classes of the generalized quaternion (or Salingaros) group, they cannot be related by TRS.
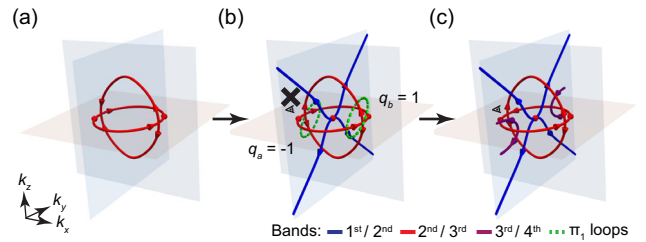

FIG. 2. Nonadjacent nodal line connection. (a) Orthogonally chained nodal rings between the 2nd and 3rd bands in the momentum space. The initial arrows (representing the non-Abelian frame charges $q = \pm g_2$) are adopted in later analyzation. (b) The arrow configuration after considering the braiding with adjacent blue nodal line, with the viewpoint indicated with an "eye" symbol. Inconsistency is found for the two TRS-related π_1 loops. (c) Possible configuration of the predicted purple nodal lines, which counterbalances the braiding induced by the blue nodal line.

Therefore, an additional topological structure must emerge to avoid this contradiction. Given the nodal structure of the 1st to 3rd bands in Fig. 2(b), one can infer that extra nodal lines are required to exist between the 3rd and 4th bands. One possible nodal line configuration to resolve the contradiction is presented in Fig. 1(d), where the vertical nodal ring is braided a second time by the purple nodal line. However, other configurations of purple nodal lines are also possible, such as the case shown in Fig. 2(c), as long as they thread through the orthogonal nodal chain to counterbalance the influence of the blue nodal line. We have hence shown that the purple nodal lines between the 3rd and 4th bands are topologically determined by the blue nodal line between the 1st and 2nd bands via interaction with the red orthogonal nodal chain from intermediate bands. These features exemplify the non-adjacent nodal line connection that incorporates the fundamental constraints on the non-Abelian frame charges from additional symmetry requirements. Such constraints should be appliable to systems with more bands or carrying other forms of nodal structure.

Metamaterial realization and experimental characterization.—We now build the metamaterial to realize the multiple nodal links system. The band structures of the metamaterial are numerically calculated (with CST Microwave studio) as shown in Fig. 3(a), where the resonators are arranged with periodicities of $p_x = 6$, $p_y = 4$, and $p_z = 3$ mm as shown in the inset. Three mirror symmetries of $M_{x,y,z}$ are kept to protect the nodal line degeneracies indicated with colored dots in Fig. 3(a) (same color convention as nodal lines). Figure 3(b) displays the BZ information highlighting the high symmetry lines. In Fig. 3(c), we show the retrieved nodal structure in the momentum space, where the multiple nodal links in the metamaterial agree well with the theoretical prediction from the effective medium model. One minor difference is in the location of the predicted nodal line between the 3rd and 4th bands, which, however, equivalently satisfies the symmetry constraints on frame charges within the multiple nodal links as the case in Figs. 1(d) or 2(c) (Supplemental Material 7 [50]). The frame charges in the real metamaterial can be numerically checked through polarization rotations (Supplemental Material 8 [50]). Interestingly, the connection between the red and purple nodal lines takes the form of in-plane chain point in Fig. 3(c). The chain point between them leads to an apparent triple degeneracy [marked with a black star in band structures of Fig. 3(a) along Γ to Y], which is in fact an approximate accidental degeneracy and the exact degeneracy can occur on fine-tuning of geometric parameters. However, the global linking between red and purple nodal lines is topologically protected. The triple degeneracy point adiabatically transforms to earring nodal links with equivalent topology when geometrical parameters change (Supplemental Material 9 [50]).
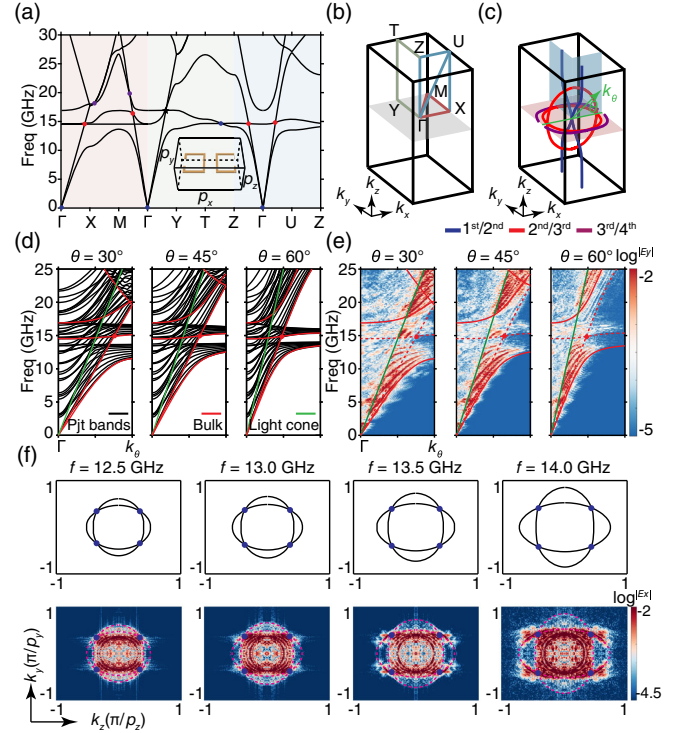

FIG. 3. Photonic metamaterial realization of multiple nodal links. (a) Band structures for the designed metamaterial (shown as inset, with background $\varepsilon_b = 2$). Resonator sizes are $L_x = 2$ mm, $L_y = 2.5$ mm, and gap $g = 1$ mm. (b) First BZ of the metamaterial. (c) Nodal structure in momentum space, with colors specifying the interacting bands. (d) Calculated band projection on the k_x-k_z plane along the k_θ directions, with θ defined in (c). (e) Experimentally measured band projections along the k_θ directions, bulk bands are shown on top as red lines. (f) Calculated and measured EFCs in the $k_y - k_z$ plane. The marked points form into the blue nodal line in (c).

The proposed metamaterial is fabricated using printed circuit boards (PCBs) technology (with a substrate material of $\varepsilon_b \approx 2$), and further experimentally characterized to examine the proposed multiple nodal links. The electromagnetic field on sample surface is measured by a microwave near-field scanning system and the measured field are Fourier transformed to retrieve the momentums space information, including the projected bands and EFCs (Supplemental Material 10 [50]). We first study the fabricated sample at the $x - z$ surface ($80 \times 10 \times 80$ units), where the vertical nodal ring in red can be experimentally observed. In Fig. 3(d), we show the calculated projected band dispersions along several θ directions [θ is defined in Fig. 3(c)]. The crossed points on the nodal ring along the θ directions are manifested as the band degeneracy positions indicated with red dots in Fig. 3(d), where the red lines represent the bulk bands on the $k_y = 0$ plane. The experimental measured results are shown in Fig. 3(e), which are in good agreement with the calculation results, and the predicted degeneracy points are indicated in red. In
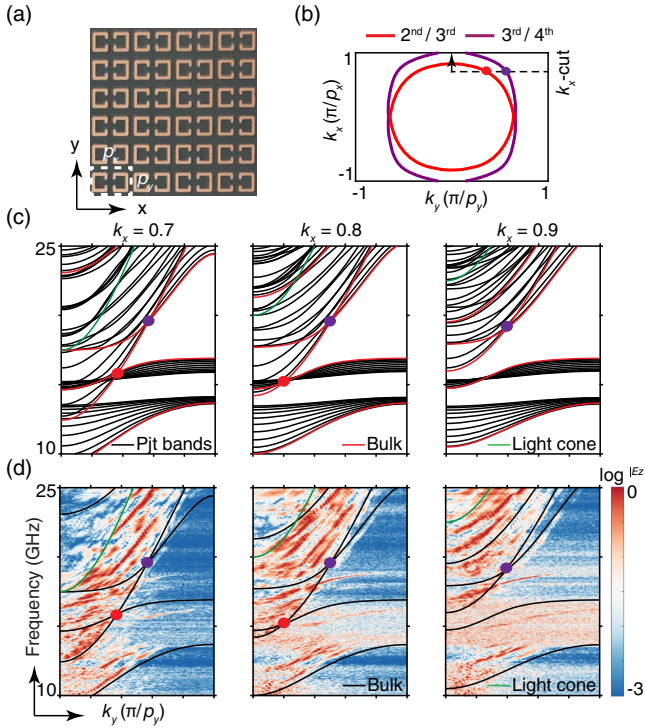
FIG. 4. Experimental verification of the nonadjacent nodal line connection. (a) Photo of the fabricated metamaterial in the $x - y$ plane. (b) Nodal structure in the $k_z = 0$ plane, the nodal ring from the 2nd and 3rd bands is shown in red, the predicted nodal lines from the 3rd and 4th bands are shown in purple. (c) Calculated band projections at fixed values of $k_x = [0.7, 0.8, 0.9] \ \pi/p_x$, where red nodal ring and purple nodal lines are manifested as colored points. Bulk bands at $k_z = 0$ plane are shown as red lines. (d) Experimentally measured band projections, with bulk bands shown in black.

addition, the light cone positions are shown as the green lines, within which the modes are leaky, and the measurement results show lower intensity.

In the first row of Fig. 3(f), we show the calculated equifrequency contours (EFCs) on the $k_y - k_z$ plane for the 1st and 2nd bands at a few frequencies (Supplemental Material 10 [50]), and the experimentally measured results on the $y - z$ sample surface ($10 \times 80 \times 80$ units) are shown in the second row. The blue nodal line in the $k_x = 0$ plane is manifested as intersection points of bulk EFCs, which can be identified from the projected band EFCs in the measured results. We have thus observed the blue nodal line formed between the 1st and 2nd bands.

With another sample surface ($80 \times 80 \times 5$ units) shown in Fig. 4(a), we characterize the nodal structures in the $k_x - k_y$ plane. The horizontal red nodal ring (formed between 2nd and 3rd bands) and the purple nodal lines (formed between 3rd and 4th bands) are shown in Fig. 4(b). To verify these two nodal lines, we cut the surface BZ at several lines corresponding to $k_x = [0.7, 0.8, 0.9] \ \pi/p_x$, where the two nodal lines are separated and can be each

identified. In Fig. 4(c), we calculated the band projection (black) and bulk bands for $k_z = 0$ (red) for such discrete k_x values (scan along k_y). The nodal points on the red nodal ring are manifested as band crossings at lower frequencies (red dots), and the nodal points from purple nodal lines can be found at higher frequencies (purple dots). In Fig. 4(d), we show the experimentally measured band projections corresponding to the calculations, where the predicted band crossings can be identified. We thus have experimentally observed the purple nodal line whose existence can be traced to the nonadjacent blue nodal line in Fig. 3(c). Further surface modes can also be found from the $x - y$ surface as presented in Supplemental Material 11 [50].

In conclusion, we have revealed the nonadjacent band gap connection in the multiple nodal links, where nodal lines from distant band pairs are topologically related through intermediate nodal structure. The experimental observation of predicted nodal lines verified the nonadjacent nodal line connection due to symmetry requirements that we proposed here. Our findings expanded the framework of non-Abelian frame charge and could motivate the exploration of further non-Abelian physics. The results establish metamaterials or photonic crystals as powerful and convenient platforms for exploring non-Abelian band topology, which may also inspire the design of new functioning topological devices.

*Corresponding author.
shuzhang@hku.hk
†Corresponding author.
phchan@ust.hk

[1] M. Z. Hasan and C. L. Kane, Colloquium: Topological insulators, Rev. Mod. Phys. **82**, 3045 (2010).

[2] L. Lu, J. D. Joannopoulos, and M. Soljačić, Topological photonics, Nat. Photonics **8**, 821 (2014).

[3] T. Ozawa, H. M. Price, A. Amo, N. Goldman, M. Hafezi, L. Lu, M. C. Rechtsman, D. Schuster, J. Simon, O. Zilberberg, and I. Carusotto, Topological photonics, Rev. Mod. Phys. **91**, 015006 (2019).

[4] L. Lu, L. Fu, J. D. Joannopoulos, and M. Soljačić, Weyl points and line nodes in gyroid photonic crystals, Nat. Photonics **7**, 294 (2013).

[5] L. Lu, Z. Wang, D. Ye, L. Ran, L. Fu, J. D. Joannopoulos, and M. Soljačić, Experimental observation of Weyl points, Science **349**, 622 (2015).

[6] M. Xiao, Q. Lin, and S. Fan, Hyperbolic Weyl Point in Reciprocal Chiral Metamaterials, Phys. Rev. Lett. **117**, 057401 (2016).

[7] W.-J. Chen, M. Xiao, and C. T. Chan, Photonic crystals possessing multiple Weyl points and the experimental

observation of robust surface states, Nat. Commun. **7**, 13038 (2016).

[8] W. Gao, B. Yang, M. Lawrence, F. Fang, B. Béri, and S. Zhang, Photonic Weyl degeneracies in magnetized plasma, Nat. Commun. **7**, 12435 (2016).

[9] D. Wang, B. Yang, W. Gao, H. Jia, Q. Yang, X. Chen, M. Wei, C. Liu, M. Navarro-Cía, J. Han, W. Zhang, and S. Zhang, Photonic Weyl points due to broken time-reversal symmetry in magnetized semiconductor, Nat. Phys. **15**, 1150 (2019).

[10] C. Fang, Y. Chen, H.-Y. Kee, and L. Fu, Topological nodal line semimetals with and without spin-orbital coupling, Phys. Rev. B **92**, 081201(R) (2015).

[11] Y. H. Chan, C.-K. Chiu, M. Y. Chou, and A. P. Schnyder, Ca_3P_2 and other topological semimetals with line nodes and drumhead surface states, Phys. Rev. B **93**, 205132 (2016).

[12] C. Fang, H. Weng, X. Dai, and Z. Fang, Topological nodal line semimetals, Chin. Phys. B **25**, 117106 (2016).

[13] H. Qiu, C. Qiu, R. Yu, M. Xiao, H. He, L. Ye, M. Ke, and Z. Liu, Straight nodal lines and waterslide surface states observed in acoustic metacrystals, Phys. Rev. B **100**, 041303(R) (2019).

[14] D. Wang, B. Yang, R.-Y. Zhang, W.-J. Chen, Z. Q. Zhang, S. Zhang, and C. T. Chan, Straight Photonic Nodal Lines with Quadrupole Berry Curvature Distribution and Superimaging "Fermi Arcs", Phys. Rev. Lett. **129**, 043602 (2022).

[15] H. Weng, Y. Liang, Q. Xu, R. Yu, Z. Fang, X. Dai, and Y. Kawazoe, Topological node-line semimetal in three-dimensional graphene networks, Phys. Rev. B **92**, 045108 (2015).

[16] R. Yu, H. Weng, Z. Fang, X. Dai, and X. Hu, Topological Node-Line Semimetal and Dirac Semimetal State in Antiperovskite Cu_3PdN, Phys. Rev. Lett. **115**, 036807 (2015).

[17] T. Bzdusek, Q. Wu, A. Ruegg, M. Sigrist, and A. A. Soluyanov, Nodal-chain metals, Nature (London) **538**, 75 (2016).

[18] T. Kawakami and X. Hu, Symmetry-guaranteed nodal-line semimetals in an fcc lattice, Phys. Rev. B **96**, 235307 (2017).

[19] R. Bi, Z. Yan, L. Lu, and Z. Wang, Nodal-knot semimetals, Phys. Rev. B **96**, 201305(R) (2017).

[20] Z. Yan, R. Bi, H. Shen, L. Lu, S.-C. Zhang, and Z. Wang, Nodal-link semimetals, Phys. Rev. B **96**, 041103(R) (2017).

[21] P.-Y. Chang and C.-H. Yee, Weyl-link semimetals, Phys. Rev. B **96**, 081114(R) (2017).

[22] J. Ahn, D. Kim, Y. Kim, and B.-J. Yang, Band Topology and Linking Structure of Nodal Line Semimetals with Z_2 Monopole Charges, Phys. Rev. Lett. **121**, 106403 (2018).

[23] W. Gao, B. Yang, B. Tremain, H. Liu, Q. Guo, L. Xia, A. P. Hibbins, and S. Zhang, Experimental observation of photonic nodal line degeneracies in metacrystals, Nat. Commun. **9**, 950 (2018).

[24] L. Xia, Q. Guo, B. Yang, J. Han, C.-X. Liu, W. Zhang, and S. Zhang, Observation of Hourglass Nodal Lines in Photonics, Phys. Rev. Lett. **122**, 103903 (2019).

[25] Q. Yan, R. Liu, Z. Yan, B. Liu, H. Chen, Z. Wang, and L. Lu, Experimental discovery of nodal chains, Nat. Phys. **14**, 461 (2018).

[26] E. Yang, B. Yang, O. You, H.-C. Chan, P. Mao, Q. Guo, S. Ma, L. Xia, D. Fan, Y. Xiang, and S. Zhang, Observation of Non-Abelian Nodal Links in Photonics, Phys. Rev. Lett. **125**, 033901 (2020).

[27] D. Wang, B. Yang, Q. Guo, R.-Y. Zhang, L. Xia, X. Su, W.-J. Chen, J. Han, S. Zhang, and C. T. Chan, Intrinsic in-plane nodal chain and generalized quaternion charge protected nodal link in photonics, Light **10**, 83 (2021).

[28] Q. Wu, A. A. Soluyanov, and T. Bzdušek, Non-Abelian band topology in noninteracting metals, Science **365**, 1273 (2019).

[29] A. Bouhon, Q. Wu, R.-J. Slager, H. Weng, O. V. Yazyev, and T. Bzdušek, Non-Abelian reciprocal braiding of Weyl points and its manifestation in ZrTe, Nat. Phys. **16**, 1137 (2020).

[30] G. E. Volovik and V. P. Mineev, Investigation of singularities in superfluid He^3 in liquid crystals by the homotopic topology methods Sov. Phys. JETP **45**, 1186 (1977), http://www.jetp.ras.ru/cgi-bin/dn/e_045_06_1186.pdf.

[31] N. D. Mermin, The topological theory of defects in ordered media, Rev. Mod. Phys. **51**, 591 (1979).

[32] G. P. Alexander, B. G.-g. Chen, E. A. Matsumoto, and R. D. Kamien, Colloquium: Disclination loops, point defects, and all that in nematic liquid crystals, Rev. Mod. Phys. **84**, 497 (2012).

[33] T. Machon and G. P. Alexander, Global defect topology in nematic liquid crystals, Proc. R. Soc. A **472**, 20160265 (2016).

[34] A. Tiwari and T. Bzdušek, Non-Abelian topology of nodal-line rings in $\mathcal{PT}$-symmetric systems, Phys. Rev. B **101**, 195130 (2020).

[35] F. N. Ünal, A. Bouhon, and R.-J. Slager, Topological Euler Class as a Dynamical Observable in Optical Lattices, Phys. Rev. Lett. **125**, 053601 (2020).

[36] P. M. Lenggenhager, X. Liu, S. S. Tsirkin, T. Neupert, and T. Bzdušek, From triple-point materials to multiband nodal links, Phys. Rev. B **103**, L121101 (2021).

[37] B. Jiang, A. Bouhon, Z.-K. Lin, X. Zhou, B. Hou, F. Li, R.-J. Slager, and J.-H. Jiang, Experimental observation of non-Abelian topological acoustic semimetals and their phase transitions, Nat. Phys. **17**, 1239 (2021).

[38] Q. Guo, T. Jiang, R.-Y. Zhang, L. Zhang, Z.-Q. Zhang, B. Yang, S. Zhang, and C. T. Chan, Experimental observation of non-Abelian topological charges and edge states, Nature (London) **594**, 195 (2021).

[39] M. Wang, S. Liu, Q. Ma, R.-Y. Zhang, D. Wang, Q. Guo, B. Yang, M. Ke, Z. Liu, and C. T. Chan, Experimental Observation of Non-Abelian Earring Nodal Links in Phononic Crystals, Phys. Rev. Lett. **128**, 246601 (2022).

[40] D. Wang, Z. Q. Zhang, and C. T. Chan, Demonstration of non-Abelian frame charge flow using photonic crystals, arXiv:2202.02978.

[41] H. Park, S. Wong, A. Bouhon, R.-J. Slager, and S. S. Oh, Topological phase transitions of non-Abelian charged nodal lines in spring-mass systems, Phys. Rev. B **105**, 214108 (2022).

[42] B. Peng, A. Bouhon, B. Monserrat, and R.-J. Slager, Phonons as a platform for non-Abelian braiding and its manifestation in layered silicates, Nat. Commun. **13**, 423 (2022).

[43] B. Jiang, A. Bouhon, S.-Q. Wu, Z.-L. Kong, Z.-K. Lin, R.-J. Slager, and J.-H. Jiang, Experimental observation of meronic topological acoustic Euler insulators, arXiv: 2205.03429.

[44] G. F. Lange, A. Bouhon, B. Monserrat, and R.-J. Slager, Topological continuum charges of acoustic phonons in two dimensions and the Nambu-Goldstone theorem, Phys. Rev. B **105**, 064301 (2022).

[45] P. M. Lenggenhager, X. Liu, T. Neupert, and T. Bzdušek, Universal higher-order bulk-boundary correspondence of triple nodal points, Phys. Rev. B **106**, 085129 (2022).

[46] J. Ahn and B.-J. Yang, Symmetry representation approach to topological invariants in $C_{2z}T$-symmetric systems, Phys. Rev. B **99**, 235125 (2019).

[47] J. Ahn, S. Park, D. Kim, Y. Kim, and B.-J. Yang, Stiefel-Whitney classes, and topological phases in band theory, Chin. Phys. B **28**, 117101 (2019).

[48] A. Bouhon and R.-J. Slager, Multi-gap topological conversion of Euler class via band-node braiding: Minimal models, PT-linked nodal rings, and chiral heirs, arXiv: 2203.16741.

[49] A. Bouhon, T. Bzdušek, and R.-J. Slager, Geometric approach to fragile topology beyond symmetry indicators, Phys. Rev. B **102**, 115135 (2020).

[50] See Supplemental Material at http://link.aps.org/supplemental/10.1103/PhysRevLett.129.263604 for derivation of effective Hamiltonian, further discussion of frame charges and multiple nodal links.

[51] I. Liberal and N. Engheta, Near-zero refractive index photonics, Nat. Photonics **11**, 149 (2017).